SUPPLEMENTARY INFORMATION

Film growth and characterization

Table S1 shows growth parameters for the films reported in this work. As-purchased substrates were loaded into our PLD chamber, then degassed at 500 °C for $SrTiO_3(001)$ and 575 °C for $MgAl_2O_4(001)$ and MgO(001). We note that degassing $SrTiO_3(001)$ at temperatures higher than 500 °C resulted in a possible surface reconstruction that was not conducive to the deposition of LiV_2O_4.

TABLE S1. Film growth parameters.

Name	Substrate	Pre-deposition temp. (°C)	Deposition temp. (°C)	Growth rate (Å/s)	Figures	Beamline
LVO75	$SrTiO_3(001)$	500	375	2.0	4 (fluorescence only)	DESY
LVO76	$SrTiO_3(001)$	500	375	2.3	2, S1, S2, S5	KARA
LVO125	$MgAl_2O_4(001)$	575	275	0.9	2–4, S1	DESY
LVO130	MgO(001)	575	275	0.3	2–4, S1	DESY
LVO146	$SrTiO_3(001)$	500	375	1.3	3, 4, S1	DESY

For the growth of LiV_2O_4 on $MgAl_2O_4(001)$ and MgO(001), the substrate temperature was held at a relatively low value of 275 °C. We found that the film quality as characterized by XRD deteriorated at higher substrate temperatures, possibly due to Mg diffusion from the substrates into the films. For the growth of LiV_2O_4 on $SrTiO_3(001)$, we found that higher substrate temperatures and faster growth rates produced better quality films with similar transport properties to that of bulk single crystals [1].

We performed XRD characterization of the films (Fig. S1) in house using a Huber four-circle diffractometer with a Cu K_α source and a Mythen 1D detector (Dectris). The full width at half maximum (FWHM) of the rocking curves is an order of magnitude larger for the relaxed films on $SrTiO_3(001)$ than the strained films on $MgAl_2O_4(001)$ and MgO(001). The relaxation produces a larger mosaic spread, which in turn reduces the effective volume of coherent x-ray scattering in the $LiV_2O_4/SrTiO_3(001)$ films, as discussed in the main text.

Determination of integrated intensity

In Figs. 3 and 4 of the main text, the x-ray scans in reciprocal space and photon energy are plotted in terms of intensity, defined as

$$\text{intensity} = \frac{\text{counts on detector}}{\text{integration time}}, \tag{S1}$$

with units of counts per second (cps). To make meaningful comparisons of the strength of the resonant forbidden (002) reflections across different films and at different azimuthal angles, we performed the following analyses: First, we normalized the counts on the detector by (1) the counts on the beam monitor at the time of data acquisition, (2) the beam attenuator factor, and (3) the film thickness. Second, we compared the area under the peak in a reciprocal-space scan along $00L$, rather than the peak intensity itself. The integrated intensity of the resonant forbidden (002) reflection (in arbitrary units) is given by

$$\text{integrated intensity} = \text{area under peak}\left[\frac{\text{counts on detector}}{\text{counts on monitor}} \times \frac{\text{attenuation factor}}{\text{film thickness}}\right]. \tag{S2}$$

To determine the areas under the peaks, we fitted each curve to the Area Gaussians function with a linear background in the PyMca software [2]. Third, we should account for the larger degree of mosaic spread in the $LiV_2O_4/SrTiO_3$ film, which reduces the effective volume that is coherently probed by x-ray scattering. To do so, we also compared integrated intensities of the resonant forbidden (002) reflection normalized by the intensity of the regular (004) reflection, as both of these scale with the effective volume that is coherently probed by x-rays.

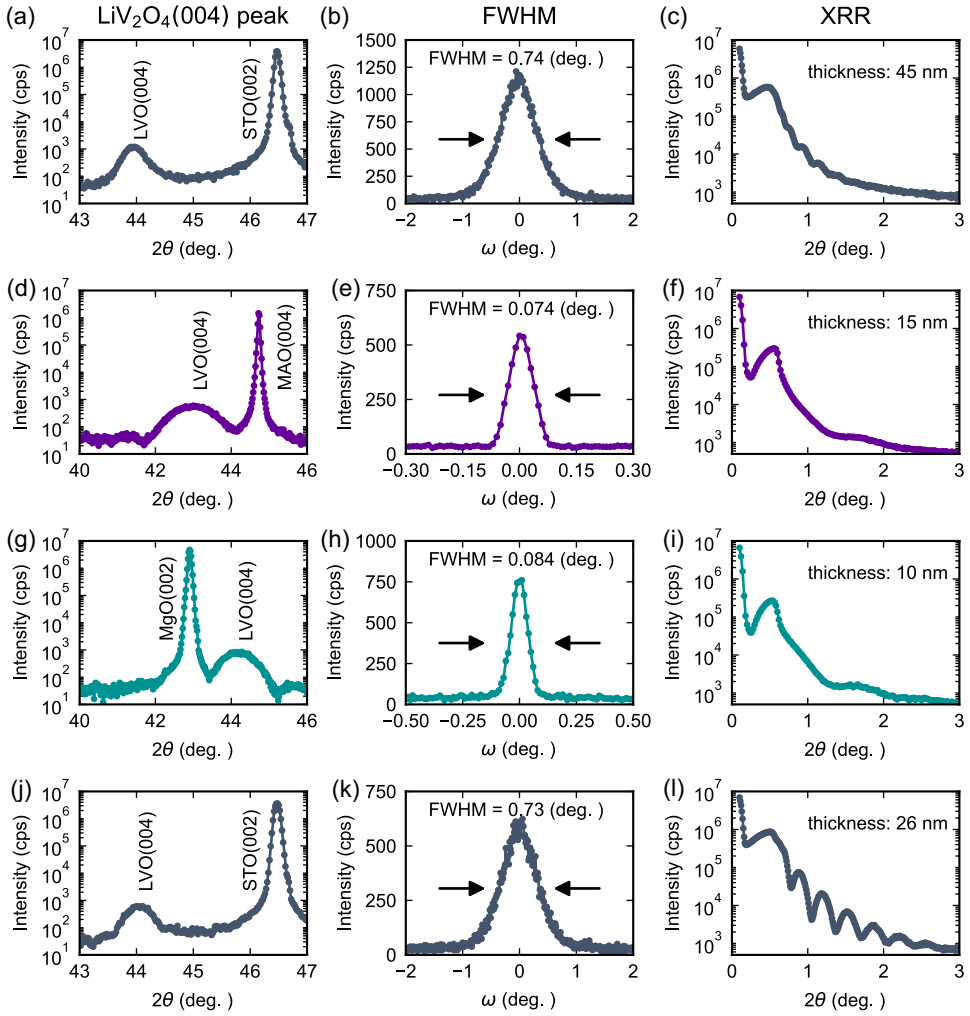

FIG. S1. XRD characterization of the films, including ω-2θ scans around the LiV_2O_4(004) reflection, rocking curves of the LiV_2O_4(004) reflection and their full width at half maximum (FWHM), and x-ray reflectivity (XRR) measurements at grazing angles, from which we extract the film thickness. (a)–(c) Sample LVO76 on $SrTiO_3$(001). (d)–(f) Sample LVO125 on $MgAl_2O_4$(001). (g)–(i) Sample LVO130 on MgO(001). (j)–(l) Sample LVO146 on $SrTiO_3$(001).

(002) reflection in the $\sigma - \sigma' + \sigma - \pi'$ channel

Figure S2 presents the azimuthal dependence of the resonant forbidden (002) reflection obtained from a second $LiV_2O_4/SrTiO_3$(001) film. The counts were acquired here without a polarization analyzer and include contributions from both the $\sigma - \sigma'$ and $\sigma - \pi'$ channels. The total intensity of the (002) reflection due to ATS scattering is given by

$$I_{002}^{\sigma-\sigma'} + I_{002}^{\sigma-\pi'} = 256|f_{xy}|^2[\sin^2(\theta) + \cos^2(\theta)\sin^2(2\varphi)]. \tag{S3}$$

Azimuthal angular dependence of the (002) reflection for tetragonal LiV_2O_4

Our derivation of the azimuthal angular and polarization dependence of the resonant forbidden (002) reflection in the main text is based on cubic LiV_2O_4 with space group $Fd\bar{3}m$. This cubic space group applies for relaxed LiV_2O_4 on $SrTiO_3$(001), but not for strained LiV_2O_4 on $MgAl_2O_4$(001) and MgO(001), which becomes tetragonal. Based on subgroup relationships, we presume that tetragonal LiV_2O_4 adopts the $I4_1/amd$ space group, similar to other

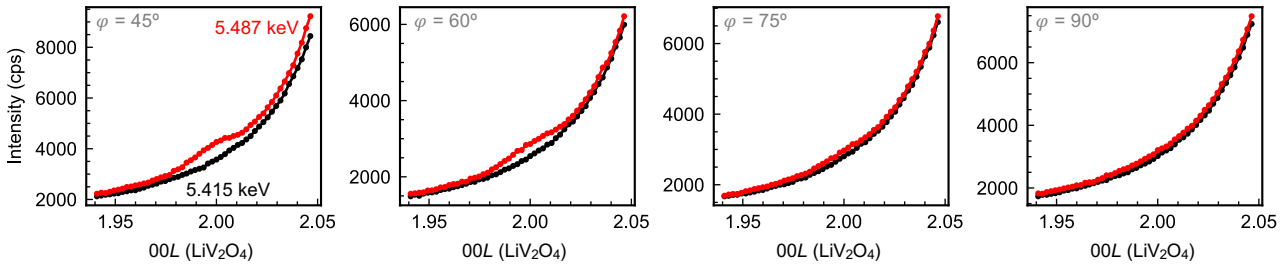

FIG. S2. Resonant forbidden (002) reflection of $LiV_2O_4/SrTiO_3$ in the $\sigma - \sigma' + \sigma - \pi'$channel, i.e., without a polarization analyzer. L-scans around (002) on and off the resonant energy at $\varphi = 45°$, 60°, 75°, and 90°. Again, the intensity of the (002) reflection is maximal at 45° and minimal at 90°.

tetragonal spinel oxides, such as $MgMn_2O_4$ [3]. The site symmetry of the V ions is reduced from $\bar{3}m$ in the cubic space group $Fd\bar{3}m$ to $2/m$ in the tetragonal space group $I4_1/amd$ [Fig. S3]. In the former, the threefold rotation axes point towards the center of the local tetrahedron, whereas in the latter, the twofold rotation axes point along the crystallographic [100] or [010] directions. From $Fd\bar{3}m$ to $I4_1/amd$, the unit cell is also reduced from $(a \times a \times a)$ to $(a/\sqrt{2} \times a/\sqrt{2} \times c)$ and rotated 45° around the [001] axis.

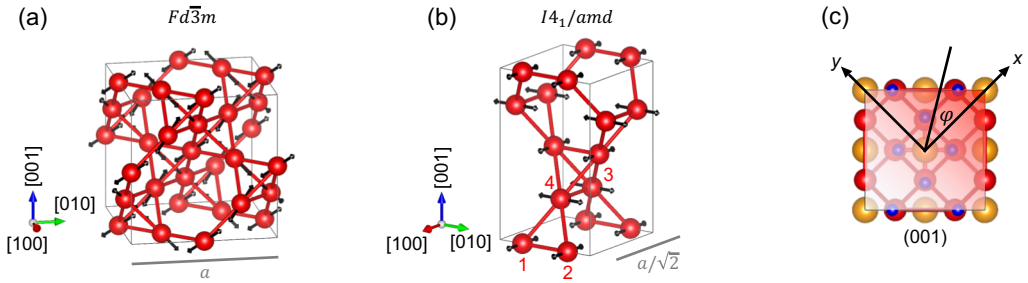

FIG. S3. (a) Cubic LiV_2O_4 with $Fd\bar{3}m$ space group. The V ions occupy the 16 c site and have $\bar{3}m$ site symmetry. The double-headed arrows mark the local threefold rotation axes. (b) Tetragonal LiV_2O_4 with $I4_1/amd$ space group. The V ions occupy the 8 c site and have $2/m$ site symmetry. The double-headed arrows mark the local twofold rotation axes. Note that the unit cell here is a $(1/\sqrt{2} \times 1/\sqrt{2} \times 1)$ reduction of that in (a) with a 45° rotation around the [001] axis. (c) For tetragonal LiV_2O_4, we define the x and y axes, as well as the azimuthal angle φ, with respect to the [100] and [010] axes of the original cubic LiV_2O_4.

The general form of the atomic form factor tensor for V ions with a twofold rotation axis along [100] is given by

$$\hat{f}_1 = \begin{pmatrix} f_{\parallel} & 0 & 0 \\ 0 & f_{\perp,11} & f_{\perp,12} \\ 0 & f_{\perp,12} & f_{\perp,22} \end{pmatrix}. \tag{S4}$$

In the frame of the enlarged unit cell equivalent to that of the original $Fd\bar{3}m$ space group, with x and y axes rotated by 45° [Fig. S3(c)], the atomic form factors for the four V ions (see Fig. S3(b) for labeling) are expressed as

$$\begin{aligned} \hat{f}_1 &= \begin{pmatrix} f_{xx} & f_{xy} & f_{xz} \\ f_{xy} & f_{xx} & f_{xz} \\ f_{xz} & f_{xz} & f_{zz} \end{pmatrix}, \ \hat{f}_2 = \begin{pmatrix} f_{xx} & f_{xy} & -f_{xz} \\ f_{xy} & f_{xx} & -f_{xz} \\ -f_{xz} & -f_{xz} & f_{zz} \end{pmatrix}, \\ \hat{f}_3 &= \begin{pmatrix} f_{xx} & -f_{xy} & f_{xz} \\ -f_{xy} & f_{xx} & -f_{xz} \\ f_{xz} & -f_{xz} & f_{zz} \end{pmatrix}, \ \hat{f}_4 = \begin{pmatrix} f_{xx} & -f_{xy} & -f_{xz} \\ -f_{xy} & f_{xx} & f_{xz} \\ -f_{xz} & f_{xz} & f_{zz} \end{pmatrix}, \end{aligned} \tag{S5}$$

where $f_{xx} = (f_{\parallel} + f_{\perp,11})/2$, $f_{xy} = (f_{\perp,11} - f_{\parallel})/2$, $f_{xz} = f_{\perp,12}/\sqrt{2}$, and $f_{zz} = f_{\perp,22}$. The structure factor at the

resonant forbidden (002) reflection is then

$$\hat{F}_{002} = 4(\hat{f}_1 + \hat{f}_2 - \hat{f}_3 - \hat{f}_4) = \begin{pmatrix} 0 & 16f_{xy} & 0 \\ 16f_{xy} & 0 & 0 \\ 0 & 0 & 0 \end{pmatrix}, \tag{S6}$$

and the intensities for the various polarization channels are

$$I_{002}^{\sigma-\sigma'} = 256|f_{xy}|^2 \sin^2(2\varphi) \tag{S7}$$

and

$$I_{002}^{\sigma-\pi'} = 256|f_{xy}|^2 \sin^2(\theta)\cos^2(2\varphi). \tag{S8}$$

We recover identical azimuthal angular and polarization dependence as that of the cubic $Fd\bar{3}m$ space group.

FDMNES simulations of REXS spectra

Table S2 reports the structural parameters used to simulate REXS spectra for the differently strained LiV_2O_4 thin films. As described in the main text, the lattice constants are determined from experiment, whereas the internal oxygen parameters are determined by structural relaxation within DFT. The $I4_1/amd$ space group for LiV_2O_4 on $MgAl_2O_4(001)$ and LiV_2O_4/MgO(001) is assumed based on the maximal symmetry allowed for tetragonal LiV_2O_4.

TABLE S2. Structural parameters for REXS simulations.

	$LiV_2O_4/MgAl_2O_4(001)$	$LiV_2O_4/SrTiO_3(001)$	LiV_2O_4/MgO(001)
Space group	$I4_1/amd$	$Fd\bar{3}m$	$I4_1/amd$
Setting	2	2	2
$a = b$ [Å]	5.717	8.240	5.957
c [Å]	8.397	8.240	8.191
Li (x y z)	.000 .750 .125	.375 .375 .375	.000 .750 .125
V (x y z)	.000 .000 .500	.000 .000 .000	.000 .000 .500
O (x y z)	.000 .485 .264	.239 .239 .239	.000 .473 .259

For the REXS simulations with FDMNES, we used the finite difference method with a cutoff radius of 5 Å and default convolution parameters. We did not observe any dipole-quadrupole contributions. We applied an additional Gaussian smoothing of width 1.25 eV to gain better resemblance to the experimental spectra. We also uniformly applied a 5 eV shift to all simulations in order to match the calculated K-edge absorption [maximum of the imaginary part of $f_{xx}(E)$] with the experimental K-edge absorption (maximum in fluorescence spectra).

Figure S4 shows the simulated atomic form factors of the V ions in the various LiV_2O_4 films. Figures S4(a)–S4(c) show the diagonal element $f_{xx}(E)$ (refer to Eq. (2) in the main text, or Eq. (S5) here), which represents some average of $f_\parallel$ and $f_\perp$, the form factor elements parallel and perpendicular to the local threefold or twofold rotation axis. The effect of strain does not produce major qualitative differences in the energy dependence of f_{xx}. We note that the intensity of the allowed (004) reflection is proportional to $|f_{xx}(E)|^2$, and its energy dependence likewise does not show much qualitative change for the different strain states.

Figures S4(d)–S4(f) show the off-diagonal element $f_{xy}(E)$, which represents the difference between $f_\parallel$ and $f_\perp$, i.e., the anisotropy of the V site. Here, the effect of strain produces notable qualitative differences in the energy dependence of f_{xy}. These differences are responsible for the changing split-peak structure in the energy dependence of the resonant forbidden (002) reflection, which is proportional to $|f_{xy}(E)|^2$.

We may summarize that changes in the *average magnitude* of the V atomic form factor in LiV_2O_4 due to epitaxial strain do not result in notable qualitative differences in REXS spectra. However, changes in the *anisotropy* of the V atomic form factor in LiV_2O_4 due to epitaxial strain are notably reflected in the resonant forbidden (002) reflection.

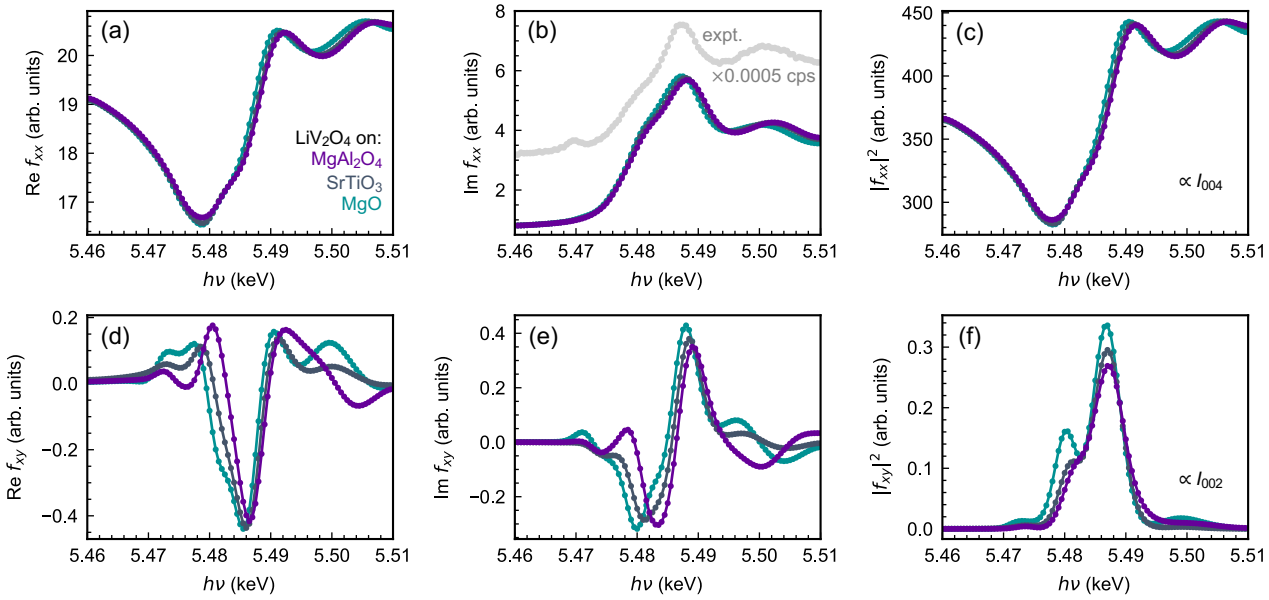

FIG. S4. FDMNES simulations of the V atomic form factor tensor in LiV_2O_4 in the different strain states induced by the substrates. (a) Real and (b) imaginary parts of the diagonal element f_{xx}. In (b), a comparison with an experimental (expt.) fluorescence spectrum of a LiV_2O_4/MgO film is shown. The experimental data is scaled by a factor of 0.0005 cps. (c) Magnitude squared of f_{xx}, which is proportional to the intensity of the (004) Bragg reflection. (d) Real and (e) imaginary parts of the off-diagonal element f_{xy}. (f) Magnitude squared of f_{xy}, which is proportional to the intensity of the resonant forbidden (002) reflection.

Rocking curves

Figure S5 shows that the extrapolated FWHM of the rocking curve for the resonant forbidden (002) reflection is broadened compared to that for the allowed (004) reflection.

Sources of experimental uncertainty

Here, we describe two sources of experimental uncertainty in the data presented in the main text.

1. X-ray scattering intensity: The total number of counts N is expected to follow a Poisson distribution with standard deviation $\sqrt{N}$. In Figs. 3(a)–3(c) and Figs. 4(a)–4(c) of the main text, the error bars $\pm\sqrt{N}$ are for the most part smaller or comparable to the size of the data points and are not shown.

2. Azimuthal dependence of integrated (002) intensity: The apparent scatter of the data in Figs. 3(d)–3(h) of the main text is not a result of fitting uncertainties. Instead, the scatter arose due to a difficulty in reproducing the exact same alignment to the substrate peak when updating the $\hat{U}\hat{B}$ matrix at each azimuthal angle ψ, given the substantial twinning seen in our substrates, particularly $MgAl_2O_4$ and $SrTiO_3$.

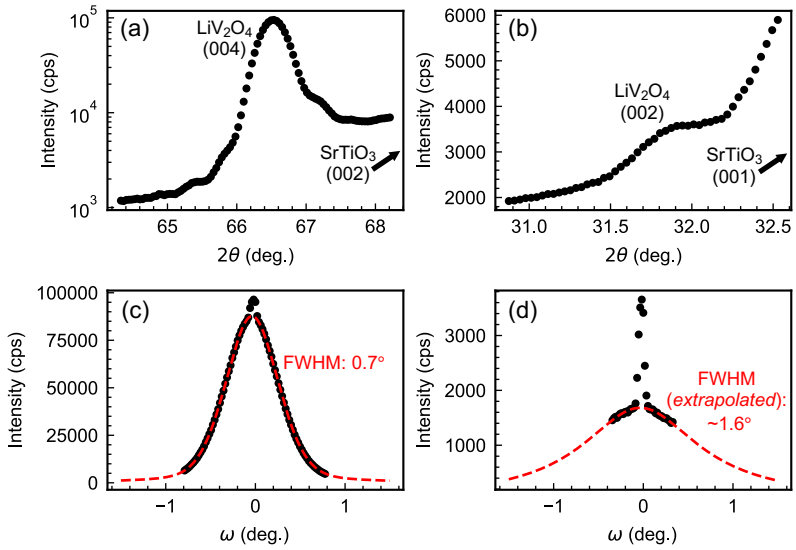

FIG. S5. ω-2θ scans around the (a) allowed (004) and (b) resonant forbidden (002) reflections of a $LiV_2O_4/SrTiO_3$ film (sample LVO76). Azimuthal angle $\varphi = 45°$; photon energy $h\nu = 5.487$ keV (on resonance). (c) and (d) Rocking curves of the (004) and (002) reflections, respectively. The dashed red lines represent fits to a Pseudo-Voigt model, and the estimated full widths at half maximum (FWHM) are shown inside the panels. There are truncation rods from nearby $SrTiO_3$ reflections, which we omitted in the fit.

[1] U. Niemann, Y.-M. Wu, R. Oka, D. Hirai, Y. Wang, Y. E. Suyolcu, M. Kim, P. A. van Aken, and H. Takagi, Crystallization of heavy fermions via epitaxial strain in spinel LiV_2O_4 thin film, Proc. Natl. Acad. Sci. U.S.A. **120**, e2215722120 (2023).
[2] V. Solé, E. Papillon, M. Cotte, P. Walter, and J. Susini, A multiplatform code for the analysis of energy-dispersive X-ray fluorescence spectra, Spectrochim. Acta Part B At. Spectrosc. **62**, 63 (2007).
[3] L. Malavasi, C. Tealdi, M. Amboage, M. C. Mozzati, and G. Flor, High pressure X-ray diffraction study of $MgMn_2O_4$ tetragonal spinel, Nucl. Instrum. Methods Phys. Res. B **238**, 171 (2005).